

Navigation in GNSS-Denied Environments Using MEMS-Grade Sensors and Geophysical Anomalies: A UKF Approach

James Brodovsky, Philip Dames, *Temple University*

BIOGRAPHY

James Brodovsky James Brodovsky is a Ph.D. candidate at Temple University in the Mechanical Engineering department, specializing in autonomous navigation within GNSS-denied environments. His research focuses on developing resilient navigation techniques for robotic, unmanned, and traditional platforms. He investigates geophysical navigation by using maps of physical phenomena to provide positioning feedback through map-matching. His most recent work explores using MEMS-grade sensors to develop methods for long-duration, GPS-denied navigation. He is the author of the open-source software library strapdown-rs, which provides a foundation for high-performance INS algorithms. He is passionate about building modern, robust, and accessible software tools for the navigation industry.

Philip Dames Philip Dames is an Associate Professor of Mechanical Engineering at Temple University. His research enables teams of mobile robots to autonomously explore and gather information with limited prior knowledge, converting sensor data into actionable intelligence. His work addresses applications including infrastructure inspection, security, mapping, environmental monitoring, precision agriculture, and search and rescue. By developing mathematical tools and systems that explicitly reason about uncertainty in environments, sensors, and robots, as well as unknown numbers of objects and unpredictable phenomena, he aims to improve robotic team performance in real-world scenarios.

ABSTRACT

This work explores the integration of open-source gravity and magnetic anomaly data into a strapdown inertial navigation system (INS) to improve navigation performance during degraded or intermittent global navigation satellite system (GNSS) availability. The primary objective is to demonstrate that a geophysical-aided INS, utilizing only low-cost micro electro-mechanical system (MEMS) grade sensors and publicly available geophysical maps, could achieve lower drift rates than a standard INS without geophysical aiding.

A comprehensive, long-term trajectory dataset (MEMS-Nav) was collected using a smartphone's internal MEMS-grade inertial measurement unit (IMU) and GNSS receiver. The GNSS data was systematically degraded using a toolbox developed by the authors to simulate GNSS interference scenarios. An INS was developed that incorporated gravity and magnetic anomaly measurements as additional aiding sources, utilizing the Institute of Geophysics and Planetary Physics (IGPP) Earth free-air anomaly map and World Digital Magnetic Anomaly Map as reference.

The geophysical-aided INS demonstrated improved navigation accuracy compared to the standard INS when operating under GNSS interference, with performance gains ranging from several meters to tens of meters on certain trajectories. Even when unable to exceed standard INS performance, the geophysical approach exhibited trends toward superior accuracy. Results showed that despite inherent MEMS-grade IMU noise and limited resolution of open-source geophysical maps, this approach demonstrates feasibility of constraining INS drift.

I. INTRODUCTION

Modern navigation systems have become critically dependent on the Global Navigation Satellite Systems (GNSS) for position corrections in inertial navigation systems (INS). While the GNSS provides accurate global positioning under ideal conditions, its reliance on radio frequency (RF) signals makes it vulnerable to denial, degradation, and spoofing in multiple scenarios (Divis, 2013; Humphreys et al., 2008; Zidan et al., 2020). Urban canyons and indoor operation obstruct satellite visibility through multipath interference or simple occlusion, while underground and underwater environments similarly occlude and attenuate GNSS signals (Cheng et al., 2018; Jalal & Nasir, 2021; Kinsey et al., 2006). More concerning are intentional disruptions: electronic warfare capabilities can actively jam or spoof GNSS signals, posing significant risks to commercial aviation, maritime shipping, and military operations (Miralles et al., 2020; Santamaria, n.d.). These vulnerabilities create an urgent need for alternative positioning, navigation, and timing (Alt-PNT) solutions that do not rely on external active RF signals.

Geophysical navigation offers a compelling non-RF alternative by exploiting naturally occurring variations in natural properties

of the Earth. In particular, Earth's gravity and magnetic fields present an opportunity due to the fact that local variation in the magnetic and gravity field—deviations from the theoretical models—are spatially correlated and mapped and as such can serve as passive navigation references. Gravity anomaly navigation compares gravimeter measurements with reference gravity maps to estimate position (Jircitano & Dosch, 1991; Kamgar-Parsi & Kamgar-Parsi, 1999; Wu et al., 2017), while magnetic anomaly navigation uses magnetometer readings matched against magnetic anomaly maps (Canciani & Raquet, 2016, 2017; Teixeira & Pascoal, 2013; Tyrén, 1982). Both approaches have been successfully demonstrated in aerospace and maritime applications, but these implementations have consistently relied on high-grade inertial measurement units (tactical or navigation-grade using ring-laser gyroscope (RLG) or fiber-optic gyroscope (FOG)) and expensive specialized sensors such as dedicated gravimeters or magnetometers.

The proliferation of micro electro-mechanical system (MEMS) sensors in smartphones, drones, and small autonomous vehicles has created a large class of low size, weight, and power (SWaP) platforms that are also conducting missions that could be subject to GNSS denial or interference. Such platforms could benefit from GNSS-independent navigation but cannot accommodate high-grade sensors due to cost or SWaP constraints. MEMS-grade IMUs (approximately \$10 to \$1,000) are orders of magnitude less expensive than tactical-grade systems (\$10,000 to \$100,000+) but suffer from substantially higher noise levels and bias instabilities. Such noise leads to rapid drift in dead-reckoning scenarios using MEMS-grade sensors. Whether geophysical anomaly navigation remains viable when using such degraded inertial sensors and publicly available, lower-resolution anomaly maps is an open question with significant practical implications. This work addresses this gap by investigating the integration of gravity and magnetic anomaly measurements directly into an Unscented Kalman Filter (UKF) based INS using only MEMS-grade sensors and open-source geophysical maps.

II. METHODOLOGY

The primary point of interest for this study is to evaluate the performance of geophysical-aided navigation under GNSS-denied conditions using low-cost MEMS-grade sensors. To this end, a geophysically-aided INS was developed using an Unscented Kalman Filter (UKF) architecture that incorporates gravity and magnetic anomaly measurements as additional aiding sources. The following subsections describe the dataset, GNSS degradation scenario, geophysical measurement models, and a UKF-based INS implementation.

1. Dataset

The dataset used for this study (Brodovsky & Dames, 2025) contains several long-duration trajectories collected using smartphone-grade MEMS IMUs and GNSS receivers via the Sensor Logger application (Choi, 2020). Each trajectory includes synchronized measurements of specific force and angular rate from the IMU, along with GNSS-derived position and velocity estimates. Additional sensors on board include a three-axis magnetometer and barometer. The trajectories were primarily collected during highway driving, providing extended periods of motion across geographically diverse regions with varying geophysical anomaly characteristics. Trajectories range from approximately 30 minutes to several hours in duration, covering distances from tens to hundreds of kilometers. The dataset provides a realistic test bed for evaluating navigation performance under GNSS-challenged conditions using low-cost sensors.

2. INS Implementation

The INS was implemented using a standard 15-state vector (9 navigation states and 6 IMU bias states).

$$\mathbf{x} = [L \quad \lambda \quad h \quad v_n \quad v_e \quad v_d \quad \phi \quad \theta \quad \psi \quad b_{a_x} \quad b_{a_y} \quad b_{a_z} \quad b_{g_x} \quad b_{g_y} \quad b_{g_z}]^\top \quad (1)$$

The INS was further augmented with gravity and magnetic anomaly bias states to incorporate geophysical aiding. Below is a brief overview of the UKF implementation.

a) IMU Error Model

The IMU error model accounts for sensor biases and noise characteristics typical of MEMS-grade sensors. The specific force and angular rate measurements from the IMU are modeled as follows:

$$\tilde{\mathbf{f}} = \mathbf{f} + \mathbf{b}_f + \mathbf{n}_f \quad (2a)$$

$$\tilde{\boldsymbol{\omega}} = \boldsymbol{\omega} + \mathbf{b}_\omega + \mathbf{n}_\omega \quad (2b)$$

where the $\tilde{\mathbf{f}}$ and $\tilde{\boldsymbol{\omega}}$ denotes the measured values, and the corresponding \mathbf{f} and $\boldsymbol{\omega}$ are the underlying true values. The accelerometer and gyroscope biases, respectively \mathbf{b}_a and \mathbf{b}_g , modeled as first-order Gauss-Markov processes. The noise terms \mathbf{n}_f and \mathbf{n}_ω are zero-mean Gaussian white noise processes with known covariance.

b) State Prediction

The UKF prediction step uses the strapdown mechanization equations (Groves, 2008, Chapter 5.3) to propagate the state estimate forward in time based on IMU measurements. The following equations describe the discrete-time updates for attitude, velocity, and position. For computational efficiency, attitude is represented using a rotation matrix \mathbf{C} from body frame to navigation (local-level) frame. The convention used is a Z-Y-X (yaw-pitch-roll) Euler angle sequence. To work with this representation, rotational rates are expressed as skew-symmetric matrices where $\boldsymbol{\omega} = [\omega_x \quad \omega_y \quad \omega_z]^\top$ corresponds to $\boldsymbol{\Omega} = \begin{bmatrix} 0 & -\omega_z & \omega_y \\ \omega_z & 0 & -\omega_x \\ -\omega_y & \omega_x & 0 \end{bmatrix}$.

First, the attitude is updated using the measured angular rates corrected for estimated biases:

$$\mathbf{C}_{t+1} \approx \mathbf{C}_t (I + \boldsymbol{\Omega}_b t) - (\boldsymbol{\Omega}_i + \boldsymbol{\Omega}_n) \mathbf{C}_t t \quad (3)$$

where $\boldsymbol{\Omega}_b$ is the skew-symmetric matrix of the body angular rates measured by the IMU corrected for estimated gyroscope biases ($\boldsymbol{\Omega}_b = [\dot{\boldsymbol{\omega}} - \mathbf{b}_\omega \wedge]$). The terms $\boldsymbol{\Omega}_i$ and $\boldsymbol{\Omega}_n$ represent the Earth's rotation rate and transport rate, respectively, expressed in the navigation frame.

Second the velocity is updated using the transformed specific force measurements:

$$\hat{\mathbf{f}}_t \approx \frac{1}{2} (\mathbf{C}_{t+1} + \mathbf{C}_t) (\mathbf{f}_t - \mathbf{b}_a) \quad (4a)$$

$$\mathbf{v}_{t+1} \approx \mathbf{v}_t + \left(\hat{\mathbf{f}}_t + \mathbf{g}_t - (2\boldsymbol{\Omega}_i + \boldsymbol{\Omega}_n) \mathbf{v}_t \right) t \quad (4b)$$

where \mathbf{g}_t is the local gravity vector at the current position, computed using the Somigliana model (Somigliana, 1929).

Finally, the position is updated using the current and previous velocity estimates, altitude first, than latitude, and longitude:

$$h_{t+1} = h_t + \frac{1}{2} (v_{d,t} + v_{d,t+1}) t \quad (5a)$$

$$L_{t+1} = L_t + \frac{1}{2} \left(\frac{v_{n,t}}{R_n(L_t) + h_t} + \frac{v_{n,t+1}}{R_n(L_t) + h_{t+1}} \right) t \quad (5b)$$

$$\lambda_{t+1} = \lambda_t + \frac{1}{2} \left(\frac{v_{e,t}}{(R_e(L_t) + h_t) \cos L_t} + \frac{v_{e,t+1}}{(R_e(L_{t+1}) + h_{t+1}) \cos L_{t+1}} \right) t \quad (5c)$$

where $R_n(L)$ and $R_e(L)$ are the meridional and transverse radii of curvature of the WGS-84 ellipsoid at latitude L .

c) Measurement Models

The standard GNSS-aided INS uses a combined position and velocity measurement model to incorporate GNSS updates. The measurement vector is defined as:

$$\mathbf{z}_{\text{GPS}} = \begin{bmatrix} L \\ \lambda \\ h \\ v_n \\ v_e \\ v_d \end{bmatrix}_{\text{GPS}} = h_{\text{GPS}}(\mathbf{x}) + \boldsymbol{\nu}_{\text{GPS}} \quad (6)$$

where $h_{\text{GPS}}(\mathbf{x})$ extracts the position and velocity components from the state vector, and $\boldsymbol{\nu}_{\text{GPS}}$ is the measurement noise, modeled as zero-mean normal distribution with covariance as reported by the accuracy measures from the GNSS receiver.

To further bound vertical position estimation, barometer measurements were integrated using a simple altitude measurement model. The onboard barometer was processed to provide a relative change in altitude measurement. This was incorporated with an initial altitude measurement from GNSS at the start of the trajectory to provide altitude updates. The barometer measurement model is defined as:

$$z_{\text{baro}} = h_{\text{baro}}(\mathbf{x}) + \boldsymbol{\nu}_{\text{baro}} \quad (7)$$

where $h_{\text{baro}}(\mathbf{x})$ extracts the altitude component from the state, and $\boldsymbol{\nu}_{\text{baro}}$ is the barometer measurement noise.

Each measurement update is processed independently within the UKF framework, allowing the filter to flexibly incorporate available aiding sources at each time step. When both GNSS and barometer measurements are available, the filter fuses all information to improve state estimation, particularly in the vertical channel where MEMS IMUs are weakest.

d) UKF INS Algorithm

The Unscented Kalman Filter (Julier & Uhlmann, 2004; E. Wan & Van Der Merwe, 2000; E. A. Wan & van der Merwe, 2001) is a nonlinear implementation of a Kalman filter that uses the unscented transform (Julier, 2002) to propagate the mean and covariance of the state distribution through nonlinear transformations. The unscented transform approximates the distribution using a set of deterministically chosen sigma points, which are propagated through the nonlinear system dynamics and measurement models. Sigma point selection is shown in Equation 8.

$$\mathcal{X}(\mathbf{x}, \mathbf{P}) = \begin{cases} \mathcal{X}_0 = \mathbf{x} \\ \mathcal{X}_i = \mathbf{x} + \left(\sqrt{(n + \lambda)\mathbf{P}} \right)_i, & i = 1, \dots, n \\ \mathcal{X}_{i+n} = \mathbf{x} - \left(\sqrt{(n + \lambda)\mathbf{P}} \right)_i, & i = 1, \dots, n \end{cases} \quad (8)$$

where \mathbf{x} is the state estimate, \mathbf{P} is the state covariance, n is the dimension of the state vector (in this case 15), and λ is a scaling parameter given by:

$$\lambda = \alpha^2(n + \kappa) - n \quad (9)$$

where α is a scaling factor (typically set to a small positive value, e.g., $1e-3$), and κ is a secondary scaling parameter (usually set to 0).

To reconstruct the mean and covariance after propagation, weights are assigned to each sigma point as follows:

$$W_0^{(m)} = \frac{\lambda}{n + \lambda} \quad (10a)$$

$$W_0^{(c)} = \frac{\lambda}{n + \lambda} + (1 - \alpha^2 + \beta) \quad (10b)$$

$$W_i^{(m)} = W_i^{(c)} = \frac{1}{2(n + \lambda)}, \quad i = 1, \dots, 2n \quad (10c)$$

where $W_i^{(m)}$ and $W_i^{(c)}$ are the weights for the mean and covariance, respectively, and β is a parameter that incorporates prior knowledge of the distribution (for normal distributions, $\beta = 2$ is optimal).

Using these sigma points and weights, the UKF modifies the standard Kalman filter prediction and update equations to handle nonlinear system dynamics and measurement models as shown in Algorithm 1 where \mathbf{Q} and \mathbf{R} are the process and measurement noise covariance matrices, respectively.

Algorithm 1 Unscented Kalman Filter (UKF) Algorithm (Thrun et al., 2005, Chapter 3.4)

- 1: $\mathcal{X}_{t-1} = \mathcal{X}(\mathbf{x}_{t-1}, \mathbf{P}_{t-1})$
 - 2: $\bar{\mathcal{X}}_{t-1} = g(\mathcal{X}_{t-1}, \mathbf{u}_{t-1})$
 - 3: $\bar{\mathbf{x}}_t = \sum_{i=0}^{2n} W^{(m)} \bar{\mathcal{X}}_t$
 - 4: $\bar{\mathbf{P}}_t = \sum_{i=0}^{2n} W^{(c)} (\bar{\mathcal{X}}_t - \bar{\mathbf{x}}_t)(\bar{\mathcal{X}}_t - \bar{\mathbf{x}}_t)^T + \mathbf{Q}$
 - 5: $\mathcal{Z}_t = h(\mathcal{X}(\bar{\mathbf{x}}_t, \bar{\mathbf{P}}_t))$
 - 6: $\bar{\mathbf{z}}_t = \sum_{i=0}^{2n} W^{(m)} \mathcal{Z}_t$
 - 7: $\mathbf{S}_t = \sum_{i=0}^{2n} W^{(c)} (\mathcal{Z}_t - \bar{\mathbf{z}}_t)(\mathcal{Z}_t - \bar{\mathbf{z}}_t)^T + \mathbf{R}$
 - 8: $\mathbf{C}_t = \sum_{i=0}^{2n} W^{(c)} (\bar{\mathcal{X}}_t - \bar{\mathbf{x}}_t)(\mathcal{Z}_t - \bar{\mathbf{z}}_t)^T$
 - 9: $\mathbf{K}_t = \mathbf{C}_t \mathbf{S}_t^{-1}$
 - 10: $\mathbf{x}_t = \bar{\mathbf{x}}_t + \mathbf{K}_t (\mathbf{z}_t - \bar{\mathbf{z}}_t)$
 - 11: $\mathbf{P}_t = \bar{\mathbf{P}}_t - \mathbf{K}_t \mathbf{S}_t \mathbf{K}_t^T$
-

3. GNSS Degradation Scenarios

To evaluate the benefit of geophysical aiding under realistic GNSS-challenged conditions, systematic degradation scenarios were applied to the GPS measurements using the `strapdown-rs` simulation toolbox (Brodovsky, 2025). The degradation framework employs an event-driven architecture that controls both measurement availability and quality through configurable schedulers and fault models.

The degradation scenario implemented a realistic model of low-quality GNSS typical of urban canyons, multipath environments, or moderate jamming conditions. Rather than simple white noise corruption, the fault model employs first-order autoregressive (AR(1)) processes to inject time-correlated errors into both position and velocity measurements. For position measurements, the AR(1) process used a correlation coefficient of $\rho_{\text{pos}} = 0.99$ and innovation standard deviation of $\sigma_{\text{pos}} = 5 \text{ m}$, creating slowly drifting biases that persist over time rather than independent random errors. The high correlation coefficient (99% retention between time steps) models realistic GNSS error characteristics where multipath or atmospheric delays change gradually. Similarly, velocity measurements were corrupted with an AR(1) process using $\rho_{\text{vel}} = 0.95$ and $\sigma_{\text{vel}} = 5 \text{ m/s}$. These correlated errors were applied independently to North, East, and vertical components, then converted to geodetic coordinates using WGS-84 ellipsoid geometry.

Additionally, the advertised measurement covariance was inflated by a factor of 15 ($r_{\text{scale}} = 15$), simulating a scenario where the GNSS receiver reports with poor accuracy estimates. This covariance inflation forces the UKF to trust degraded GNSS measurements less than it should based on nominal accuracies, representing realistic receiver behavior under signal degradation where dilution of precision (DOP) values may not fully capture measurement quality. The combination of correlated measurement errors and inflated covariance creates a challenging navigation scenario that stresses the filter's ability to maintain accurate state estimates.

All degradation parameters were applied identically to both the GPS-degraded and geophysically-aided configurations to ensure a controlled comparison. The geophysically-aided system received gravity and magnetic anomaly measurements at the IMU update rate, providing continuous alternative position information to complement the degraded GNSS observations.

4. Augmented UKF with Geophysical Aiding

The geophysically-aided INS extends the standard 15-state UKF INS by incorporating geophysical anomaly measurements as an additional aiding source. The state vector retains the existing 15 canonical states, with the addition of an additional bias state corresponding to the anomaly in question. Gravity and magnetic anomaly measurements are processed independently, each with its own measurement model and noise characteristics.

Geophysical anomaly measurements were derived by comparing sensed quantities with values predicted from publicly available global anomaly maps. For gravity anomalies, we used the Institute of Geophysics and Planetary Physics (IGPP) Earth Free-air Anomaly free-air anomaly map (Pavlis et al., 2012), which provides gravity anomaly values at a resolution of approximately 1 arc-minute (approximately 1.8 km at the equator). For magnetic anomalies, the World Digital Magnetic Anomaly Map (WDMAM) (Lesur et al., 2016) was used, offering anomaly data at a resolution of 3 arc-minutes (approximately 5.6 km at the equator). Both were accessed via the Generic Mapping Tools (GMT) software package (Wessel et al., 2019). GMT provides tools for querying the maps based on latitude (L) and longitude (λ) coordinates, returning bilinearly interpolated anomaly values at arbitrary positions. This allows for a straightforward implementation of the measurement models within the UKF framework: $h(\mathbf{x}) = \text{map}(L, \lambda)$.

To develop the corresponding sensor models, the sensed gravity and magnetic field values were first converted to anomaly residuals by subtracting the theoretical model values at the current estimated position. This yields two distributions of measurement residuals that can be roughly approximated as a normal distribution. Notably, these are not zero-mean as is required by a Kalman-family filter. To address this, the measurement model first adds a bias state to the UKF state vector, allowing the filter to learn and compensate for systematic offsets between measured and mapped anomalies over time. The normal distribution parameters are shown in Table 1.

Table 1: Geophysical Anomaly Measurement Model Parameters

Anomaly Type	Mean Residual	Std. Deviation
Gravity Anomaly	16.62 mGal	23.62 mGal
Magnetic Anomaly	-20.64 nT	124.69 nT

To characterize the measurement noise statistics, the difference between measured and mapped anomalies was computed along each reference trajectory. The resulting residual distribution was analyzed and found to be approximately Gaussian. The sample mean and standard deviation of these residuals informed the measurement noise covariance matrix used in the UKF. This empirical characterization accounts for both sensor noise, map errors, and interpolation uncertainties inherent in the anomaly matching process.

5. Performance Evaluation

Navigation performance was evaluated by comparing the estimated trajectories from each INS configuration against the raw GNSS measurements collected during the reference data collection. Two primary INS configurations were tested under degraded

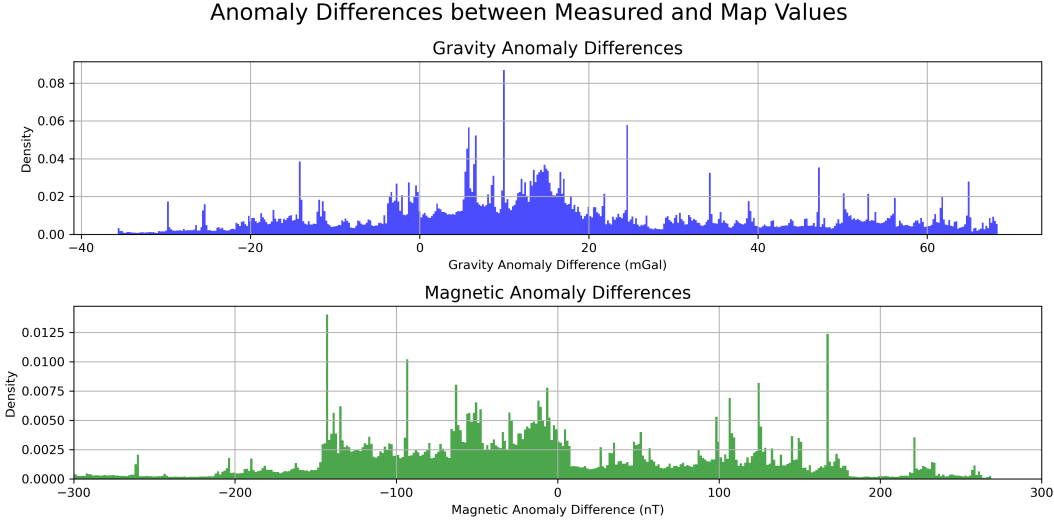


Figure 1: Statistical analysis of gravity and magnetic anomaly measurement residuals along reference trajectories.

GNSS conditions: a standard GNSS-degraded INS without geophysical aiding, and a geophysically-aided INS that incorporated gravity and magnetic anomaly measurements. Both configurations processed the same degraded GNSS measurements (with AR(1) correlated errors and $15\times$ covariance inflation).

Position error was quantified using the haversine distance formula, which computes the great-circle distance between two points on a sphere given their latitude and longitude coordinates. For estimated position (L_1, λ_1) and reference GNSS position (L_2, λ_2) , the haversine distance is:

$$d = 2R \arcsin \left(\sqrt{\sin^2 \left(\frac{L_2 - L_1}{2} \right) + \cos(L_1) \cos(\phi_2) \sin^2 \left(\frac{\lambda_2 - \lambda_1}{2} \right)} \right) \quad (11)$$

where $R = 6371$ km is the Earth's mean radius, L represents latitude in radians, and λ represents longitude in radians. This metric provides geodetically accurate position errors accounting for Earth's curvature, particularly important for the long-distance trajectories in the MEMS-Nav dataset.

The relative performance improvement was assessed by computing the difference in position error between the GNSS-degraded INS and the geophysically-aided INS at each time step. A negative difference indicates that the geophysically-aided system achieved lower error than the GNSS-only system, demonstrating the benefit of incorporating geophysical anomaly measurements. Performance metrics including mean error, root-mean-square error (RMSE), maximum error, and cumulative error distributions were computed across all trajectories to quantify the effectiveness of geophysical aiding under realistic GNSS-challenged conditions.

III. RESULTS

The geophysically-aided INS was evaluated across 13 trajectories from the MEMS-Nav dataset by comparing navigation performance against a GNSS-degraded baseline INS without geophysical aiding. Tables 2 and 3 present position error differences computed as the baseline error minus the geophysically-aided error, where negative values indicate improvement (lower error) with geophysical aiding. Position errors were computed using the haversine distance formula, with statistics aggregated to assess the overall effectiveness and consistency of geophysical anomaly integration under GNSS-challenged conditions.

Table 2 presents the performance differential for gravity anomaly-aided navigation relative to the GNSS-degraded baseline. Of the 13 trajectories evaluated, 6 showed improvement with gravity aiding (negative error differences), while 7 exhibited degraded performance. The inconsistency is striking: trajectories with successful gravity aiding achieved substantial error reductions, with the best case (2023-08-04_214758) demonstrating an 841.3 m reduction in RMSE and 343.8 m reduction in drift. Similarly, trajectory 2025-07-31_23-36-03 showed 680.3 m RMSE improvement with 182.1 m drift reduction. Conversely, trajectories where gravity aiding failed showed significant performance degradation, most notably 2023-08-09_163741 with an 8430.6 m

Table 2: Gravity Anomaly-Aided Navigation Position Error Statistics (meters)

Trajectory	RMSE	Mean	Median	Drift
2025-06-18_15-09-25	976.6	629.1	262.6	658.2
2025-09-27_18-10-16	-403.8	-61.4	-16.1	-531.4
2025-07-31_23-36-03	-680.3	-459.5	-117.2	-182.1
2025-03-01_150426	385.7	498.1	413.0	254.9
2025-06-27_11-54-35	-565.9	-318.3	-165.4	-114.4
2025-07-04_17-24-46	205.8	-108.3	-39.7	118.2
2023-08-06_144805	-70.3	-46.1	-34.4	-28.4
2025-03-01_164639	359.8	458.8	239.3	241.4
2025-09-26_19-03-38	1353.1	987.1	340.6	294.8
2025-06-18_16-52-32	58.3	27.6	-0.2	26.5
2023-08-04_214758	-841.3	-10.95	-25.3	-343.8
2023-08-09_163741	8430.6	1123.0	41.2	11768.3
2025-07-18_23-13-43	-8.4	-4.25	-1.0	-5.4
Mean	707.7	208.8	72.9	935.1
Std Dev	2309.4	468.5	173.2	3140.7

Table 3: Magnetic Anomaly-Aided Navigation Position Error Statistics (meters)

Trajectory	RMSE	Mean	Median	Drift
2025-06-18_15-09-25	2571.9	2054.0	1438.6	1733.6
2025-09-27_18-10-16	717.9	1279.5	1387.4	944.6
2025-07-31_23-36-03	-644.2	-412.3	-82.8	-172.5
2025-03-01_150426	175.2	182.5	136.8	115.8
2025-06-27_11-54-35	-550.9	-402.5	-215.2	-111.3
2025-07-04_17-24-46	-160.6	-153.5	-6.9	-92.2
2023-08-06_144805	46.3	27.9	44.7	18.7
2025-03-01_164639	149.3	191.7	198.1	100.2
2025-09-26_19-03-38	225.5	284.6	140.1	49.1
2025-06-18_16-52-32	15.0	43.6	0.4	6.8
2023-08-04_214758	375.2	1788.1	201.8	153.3
2023-08-09_163741	8306.6	938.4	69.0	11595.0
2025-07-18_23-13-43	222.1	100.4	6.3	143.8
Mean	880.7	455.6	244.6	1114.2
Std Dev	2271.7	772.4	511.0	3067.5

increase in RMSE and catastrophic 11.8 km drift increase. The mean RMSE difference of 707.7 m (positive) with standard deviation of 2309.4 m reflects this high variability, indicating that while gravity aiding shows promise in favorable conditions, its benefits are highly geography-dependent.

Table 3 shows similar patterns for magnetic anomaly-aided navigation, though with slightly different trajectory-specific performance. Three trajectories demonstrated improvement with magnetic aiding, while seven showed degradation. The most successful cases achieved meaningful error reductions: trajectory 2025-07-31_23-36-03 showed 644.2 m RMSE improvement and 172.5 m drift reduction, while 2025-06-27_11-54-35 exhibited 550.9 m RMSE improvement with 111.3 m drift reduction. However, the worst-performing trajectory 2023-08-09_163741 again suffered catastrophic degradation with 8306.6 m RMSE increase and 11.6 km drift increase. The mean RMSE difference of 880.7 m with standard deviation of 2271.7 m confirms the inconsistent nature of magnetic anomaly aiding, though slightly worse on average than gravity aiding.

Comparing the two geophysical modalities reveals similar inconsistency patterns but with different geographic sensitivities. Gravity aiding performed better on average (707.7 m vs. 880.7 m mean RMSE difference) and showed improvement on one additional trajectory compared to magnetic aiding. Notably, some trajectories benefited from one modality but not the other: trajectory 2025-07-04_17-24-46 showed 160.6 m magnetic improvement but 205.8 m gravity degradation, while 2023-08-06_144805 exhibited 70.3 m gravity improvement but 46.3 m magnetic degradation. This suggests complementary information content, where local anomaly field characteristics determine which modality provides effective navigation constraints. The catastrophic failures on trajectories like 2023-08-09_163741 for both modalities indicate fundamental challenges—likely geophysically homogeneous regions with insufficient spatial variation, poor map quality in those areas, or unmodeled systematic biases that caused filter divergence rather than convergence.

IV. CONCLUSION

This work demonstrates that geophysical anomaly-aided navigation using only MEMS-grade sensors and publicly available geophysical maps is capable of improving navigation accuracy under GNSS-degraded conditions. This represents a significant departure from prior geophysical navigation research, which has consistently relied on tactical or navigation-grade IMUs costing tens to hundreds of thousands of dollars and specialized sensors such as dedicated gravimeters or cesium-vapor magnetometers. By successfully demonstrating error reductions ranging from tens to hundreds of meters on approximately half of the evaluated trajectories using commodity smartphone sensors and open-source anomaly maps, this research establishes the fundamental feasibility of extending geophysical navigation from high-grade military and aerospace systems to mass-market consumer and commercial platforms.

The results reveal both the promise and the limitations of low-cost geophysical navigation. When conditions are favorable—trajectories through regions with strong, well-mapped geophysical gradients—both gravity and magnetic anomaly aiding achieved substantial performance improvements, with some cases showing RMSE reductions exceeding 800 meters and drift reductions of several hundred meters compared to GNSS-degraded baselines. The best-performing trajectories demonstrated that MEMS-grade sensors paired with 1-3 arc-minute resolution anomaly maps can provide meaningful navigation constraints even under severe GNSS degradation (AR(1) correlated errors plus 15 \times covariance inflation). However, performance was highly inconsistent and geography-dependent: approximately half of the trajectories showed no benefit or active degradation, with catastrophic failures exhibiting multi-kilometer drift increases. This inconsistency stems from spatially varying anomaly field strength and map quality, where geophysically homogeneous regions or areas with poor map coverage provide insufficient observability for the UKF to converge effectively.

The complementary nature of gravity and magnetic modalities suggests potential for further improvement through multi-modal sensor fusion. Several trajectories benefited from one geophysical modality while degrading with the other, indicating that local anomaly field characteristics determine which measurements provide effective navigation constraints. A combined approach that intelligently weights or selects between modalities based on estimated anomaly field gradients and filter innovation statistics could potentially improve consistency. Additionally, the catastrophic failure modes observed on certain trajectories highlight the need for anomaly field observability analysis and integrity monitoring—the filter should detect when geophysical measurements provide insufficient information and gracefully degrade to dead-reckoning or rely more heavily on available GNSS measurements rather than diverging.

The practical implications of this work are significant for the Alt-PNT ecosystem. While geophysical navigation with MEMS sensors cannot yet match the reliability or accuracy of high-grade implementations, it provides a low-cost, passive, non-RF alternative that could augment existing navigation systems on size, weight, power, and cost-constrained platforms including smartphones, commercial drones, small autonomous vehicles, and wearable devices. The demonstrated error reductions of tens to hundreds of meters extend the viable operating time under GNSS denial from minutes to potentially hours for applications with modest accuracy requirements. For safety-critical applications, geophysical measurements could serve as an additional integrity check against GNSS spoofing or jamming, where sudden large deviations between GNSS-derived position and geophysically-inferred position would trigger alerts.

Future work should address several key limitations identified in this study. First, the inconsistent performance demands better understanding of which geographic regions and trajectory characteristics enable successful geophysical navigation. Predictive models that map expected navigation performance based on local anomaly field properties and map quality could guide mission planning and enable adaptive filter configurations. Second, the filter framework requires improved robustness through anomaly field observability metrics, integrity monitoring, and adaptive measurement weighting that responds to local field conditions. Third, exploration of additional geophysical phenomena (e.g., terrain-aided navigation, magnetic field vector matching, or multiscale anomaly representations) may provide complementary information that improves consistency. Finally, validation on additional sensor platforms, geographic regions, and trajectory types will better characterize the operational envelope of low-cost geophysical navigation.

This research establishes that improving GNSS-denied navigation using MEMS-grade sensors and geophysical anomaly maps is not only possible but achievable with existing open-source data and commodity hardware. While significant work remains to improve consistency and reliability, the demonstrated capability opens a new avenue for resilient, low-cost navigation solutions that reduce dependence on vulnerable RF-based positioning systems. As MEMS sensor technology continues to improve and higher-resolution anomaly maps become available, geophysical navigation may transition from a niche military and aerospace capability to a practical augmentation for mass-market navigation systems.

ACKNOWLEDGEMENTS

The authors would like to acknowledge the support and assistance of Beth Brodovsky, Jeremy Brodovsky, Monica Brodovsky, Bill Siegl, and Alkesh Kumar Srivastava for their help in data collection efforts.

REFERENCES

- Brodovsky, J. (2025). *Strapdown-rs: A simple strapdown INS implementation in rust*. <https://doi.org/10.5281/zenodo.1234567>
- Brodovsky, J., & Dames, P. (2025). *MEMS-Nav: A MEMS-grade dataset for navigation research*. <https://doi.org/10.5281/zenodo.17582434>
- Canciani, A., & Raquet, J. (2016). Absolute positioning using the earth's magnetic anomaly field. *NAVIGATION: Journal of the Institute of Navigation*, 63(2), 111–126.
- Canciani, A., & Raquet, J. (2017). Airborne magnetic anomaly navigation. *IEEE Transactions on aerospace and electronic systems*, 53(1), 67–80.
- Cheng, J., Cheng, H., Meng, M. Q.-H., & Zhang, H. (2018). Autonomous navigation by mobile robots in human environments: A survey. *2018 IEEE International Conference on Robotics and Biomimetics (ROBIO)*, 1981–1986. <https://doi.org/10.1109/ROBIO.2018.8665075>
- Choi, T. H. (2020). *Awesome sensor logger* (tech. rep.). <https://github.com/tszheichoi/awesome-sensor-logger>
- Divis, D. A. (2013). Gps spoofing experiment knocks ship off course. *Inside GNSS*, 31, 1–3.
- Groves, P. D. (2008). *Principles of gnss, inertial, and multisensor integrated navigation systems*. Artech House.
- Humphreys, T. E., Ledvina, B. M., Psiaki, M. L., O'Hanlon, B. W., & Kintner, P. M. (2008). Assessing the spoofing threat: Development of a portable GPS civilianspoof. *Proceedings of the ION GNSS international technical meeting of the satellite division*, 21, 2314–2325.
- Jalal, F., & Nasir, F. (2021). Underwater navigation, localization and path planning for autonomous vehicles: A review. *2021 International Bhurban Conference on Applied Sciences and Technologies (IBCAST)*, 817–828. <https://doi.org/10.1109/IBCAST51254.2021.9393315>
- Jircitano, A., & Dosch, D. E. (1991). Gravity aided inertial navigation system (gains). *Proceedings of the 47th Annual Meeting of The Institute of Navigation (1991)*, 221–229.
- Julier, S. (2002). The scaled unscented transformation. *Proceedings of the 2002 American Control Conference (IEEE Cat. No.CH37301)*, 6, 4555–4559 vol.6. <https://doi.org/10.1109/ACC.2002.1025369>
- Julier, S., & Uhlmann, J. (2004). Unscented filtering and nonlinear estimation. *Proceedings of the IEEE*, 92(3), 401–422. <https://doi.org/10.1109/JPROC.2003.823141>
- Kamgar-Parsi, B., & Kamgar-Parsi, B. (1999). Vehicle localization on gravity maps. *Unmanned ground vehicle technology*, 3693, 182–191.
- Kinsey, J. C., Eustice, R. M., & Whitcomb, L. L. (2006). A survey of underwater vehicle navigation: Recent advances and new challenges. *IFAC conference of manoeuvering and control of marine craft*, 88, 1–12.
- Lesur, V., Hamoudi, M., Choi, Y., Dyment, J., & Thébault, E. (2016). Building the second version of the world digital magnetic anomaly map (wdmam). *Earth, Planets and Space*, 68(1), 27.
- Miralles, D., Bornot, A., Rouquette, P., Levigne, N., Akos, D. M., Chen, Y.-H., Lo, S., & Walter, T. (2020). An assessment of gps spoofing detection via radio power and signal quality monitoring for aviation safety operations. *IEEE Intelligent Transportation Systems Magazine*, 12(3), 136–146. <https://doi.org/10.1109/MITS.2020.2994117>
- Pavlis, N. K., Holmes, S. A., Kenyon, S. C., & Factor, J. K. (2012). The development and evaluation of the earth gravitational model 2008 (egm2008). *Journal of Geophysical Research: Solid Earth*, 117(B4). <https://doi.org/10.1029/2011JB008916>
- Santamaría, E. (n.d.). Global navigation satellite system GNSS radio frequency interference.
- Somigliana, C. (1929). Teoria generale del campo gravitazionale dell'ellissoide di rotazione. *Memorie della Società Astronomia Italiana*, Vol. 4, p. 425, 4, 425.
- Teixeira, F. C., & Pascoal, A. (2013). Magnetic navigation and tracking of underwater vehicles [9th IFAC Conference on Control Applications in Marine Systems]. *IFAC Proceedings Volumes*, 46(33), 239–244. <https://doi.org/10.3182/20130918-4-JP-3022.00059>
- Thrun, S., Burgard, W., & Fox, D. (2005). *Probabilistic robotics*. MIT Press.
- Tyrén, C. (1982). Magnetic anomalies as a reference for ground-speed and map-matching navigation. *The Journal of navigation*, 35(2), 242–254.
- Wan, E., & Van Der Merwe, R. (2000). The unscented kalman filter for nonlinear estimation. *Proceedings of the IEEE 2000 Adaptive Systems for Signal Processing, Communications, and Control Symposium (Cat. No.00EX373)*, 153–158. <https://doi.org/10.1109/ASSPCC.2000.882463>
- Wan, E. A., & van der Merwe, R. (2001). The unscented kalman filter. In *Kalman filtering and neural networks* (pp. 221–280). John Wiley; Sons, Ltd. <https://doi.org/https://doi.org/10.1002/0471221546.ch7>
- Wessel, P., Luis, J. F., Uieda, L., Scharroo, R., Wobbe, F., Smith, W. H. F., & Tian, D. (2019). The generic mapping tools version 6. *Geochemistry, Geophysics, Geosystems*, 20(11), 5556–5564. <https://doi.org/https://doi.org/10.1029/2019GC008515>
- Wu, L., Wang, H., Chai, H., Zhang, L., Hsu, H., & Wang, Y. (2017). Performance evaluation and analysis for gravity matching aided navigation. *Sensors*, 17(4). <https://doi.org/10.3390/s17040769>
- Zidan, J., Adegoke, E., Kampert, E., Birrell, S., Ford, C., & Higgins, M. (2020). Gnss vulnerabilities and existing solutions: A review of the literature. *IEEE Access*, PP, 1–1. <https://doi.org/10.1109/ACCESS.2020.2973759>